JM PAPERS

Creation of quantum knots and links driven by minimal surfaces

Simone Zuccher[1] **and Renzo L. Ricca**[2,3,†]

[1]Department of Computer Science, U. Verona, Ca' Vignal 2, Strada Le Grazie 15, 37134 Verona, Italy

[2]Department of Mathematics and Applications, University of Milano-Bicocca, Via Cozzi 55, 20125 Milano, Italy

[3]BDIC, Beijing U. Technology, 100 Pingleyuan, Beijing 100124, PR China

Using an improved numerical code we investigate the creation and evolution of quantum knots and links as defects of the Gross–Pitaevskii equation. The particular constraints put on quantum hydrodynamics make this an ideal context for application of geometric and topological methods to investigate dynamical properties. Evolutionary processes are classified into three generic scenarios representing (i) direct topological cascade and collapse, (ii) structural and topological cycles, and (iii) inverse topological cascade of complex structures. Several examples and test cases are studied; the head-on collision of quantum vortex rings and the creation of a trefoil knot from initially unlinked, unknotted loops are realized for the first time. Each type of scenario is studied by carrying out a detailed evaluation of fundamental geometric and dynamical properties associated with evolution. Direct topological cascade that governs the decay of complex structures to small-scale vortex rings is identified by writhe measures, while picks of total curvature are found to provide a clear signature of reconnection events. We demonstrate that isophase minimal surfaces spanning knots and links have a privileged role in the decay process by detecting surface energy relaxation of complex structures. Minimal surfaces are shown to be critical markers for energy and prove to be appropriate detectors for the evolution of complex systems.

1. Introduction

In this paper, by analysing the creation and evolution of vortex knots and links under the Gross–Pitaevskii equation (GPE) we show that total curvature and writhing number prove to be appropriate detectors for reconnection events and production of small-scale vortex

rings, and we demonstrate that minimal isophase surfaces are privileged markers in the decay process and surface energy relaxation of complex structures.

Since the first experimental realizations of Bose–Einstein condensates (Andrews *et al.* 1997; Cornell & Wieman 1998), quantum defects have become objects of intense study for their fundamental aspects in science and their potential role in future technology. Laboratory creation of quantum vortices is part of current research (Matthews *et al.* 1999; Leanhardt *et al.* 2002) and theoretical work, based also on the advances of numerical simulations (Wyatt 2005; Caliari & Zuccher 2021), is pushing the limits to explore new states of matter where defects may form complex networks of knots and links (Hall *et al.* 2016; Kleckner, Kauffman & Irvine 2016; Zuccher & Ricca 2017; Foresti & Ricca 2019). By relying on the progress made in the field, we exploit here the constraints posed by quantum hydrodynamics to investigate and determine new relationships between geometric and topological properties associated with creation and evolution of quantum knots and links and key features of evolutionary processes and energy transfers.

To place all this in context, let us consider a condensate given by a highly diluted gas of bosons in an unbounded domain at ultra-cold temperature (Pitaevskii & Stringari 2016). In this situation particles loose their independence and are governed by a single wavefunction $\psi = \psi(\boldsymbol{x}, t)$, $\boldsymbol{x}$ being vector position and t time. By taking into account only first-order effects, the system is governed by a mean field equation given by the GPE (Gross 1961; Pitaevskii 1961) that in non-dimensional form reads as

$$\frac{\partial \psi}{\partial t} = \frac{\mathrm{i}}{2} \nabla^2 \psi + \frac{\mathrm{i}}{2} \left(1 - |\psi|^2 \right) \psi. \tag{1.1}$$

This system admits defects that emerge as nodal lines of the wavefunction. By applying the Madelung transformation $\psi = \sqrt{\rho} \exp(\mathrm{i}\theta)$ (θ phase of ψ), the imaginary and real parts of (1.1) are transformed into a momentum and a continuity equation of a fluid-like medium of density $\rho = |\psi|^2$ and velocity $\boldsymbol{u} = \nabla\theta$; we take $\rho \to 1$ as $|\boldsymbol{x}| \to \infty$. This allows us to interpret the evolution of the condensate by a hydrodynamic description, where continuity is governed by the standard equation of a compressible fluid, and momentum is purely balanced by density gradients (Barenghi & Parker 2016). The viscous term of ordinary fluids is thus replaced by the action of a quantum potential that to some extent makes the dynamics of the system similar to that of an Euler flow. The presence of a quantum potential not only makes particle trajectories highly correlated, but it also introduces a form of memory of the initial conditions in the wave function (Wyatt 2005). In many respects, at least to first approximation, the world of quantum hydrodynamics is much simpler than that of a classical, viscous fluid. Hence, the presence of quantum defects makes this system all the more interesting because, contrary to the Euler context, vortex defects are objects strictly localized that can reconnect and change topology in the absence of dissipation.

Relationships between topological aspects and non-Hermiticity properties of the governing Hamiltonian (related to local energy loss and gain, twist and writhe production, and stability analysis) are currently under intense investigation for both theoretical aspects and practical applications (Dos Santos 2016; Zuccher & Ricca 2018; Foresti & Ricca 2019, 2020; Coulais, Fleury & van Wezel 2021; Wang *et al.* 2021), and this justifies the present study. The paper is organized as follows. Key results in topological quantum hydrodynamics are presented in § 2, where we propose to classify evolutionary processes under three topologically distinct scenarios, useful for investigation. In § 3 we give some information on the numerical method and implementation for measuring geometric and topological quantities. In § 4 we consider several test cases according to the three scenarios identified in § 2. Results regarding total length, curvature, writhe, twist and kinetic helicity

are presented and discussed in §5. In §6 we recall various energy contributions and evaluate the relevant terms considering isophase surfaces of least geometric area, proving that these minimal surfaces have indeed a privileged role in the decay process and surface energy relaxation of complex structures. Conclusions are drawn in §7

2. Topological quantum hydrodynamics

We identify a defect line with an oriented space curve $\mathcal{C}$ in $\mathbb{R}^3$ represented by the vector position X; vorticity $\boldsymbol{\omega}$ is given by a Dirac delta function $\boldsymbol{\delta}(X)$ that induces the orientation on $\mathcal{C}$. A nodal line can thus be seen as a locus of intersection of infinitely many phase surfaces S. Since by definition a Seifert surface of a knot is a (compact, connected) oriented surface in $\mathbb{R}^3$ whose boundary is the given knot (Rolfsen 1990), any surface S of constant phase (isophase) spanning $\mathcal{C}$ is a Seifert surface of $\mathcal{C}$; isophase surfaces of defects are therefore Seifert surfaces whose orientation is induced by vorticity. An example of such a surface for the Hopf link is shown in figure 10(*a*) of §6.

Quantum defects have quantized circulation given by $\Gamma = 2\pi n$ ($n \in \mathbb{N}$), where n denotes topological charge (non-dimensionalized by $\hbar/m$, where $\hbar = h/2\pi$, with h Planck's constant and m the particle's mass). Quantization arises from the line integration of $\boldsymbol{u} = \nabla\theta$ over a loop encircling $\mathcal{C}$ once and multivaluedness of the phase θ. For simplicity and without loss of generality, we shall take $n = 1$. By application of Noether's theorem, circulation emerges as the first conserved charge of quantum fluids (Kedia *et al.* 2018) and can be regarded as a topological invariant of the system. Together with other conserved quantities like total mass and energy, a second conserved quantity of topological character is kinetic helicity; classically this is defined by

$$\mathcal{H} = \int_{\Omega} \boldsymbol{u} \cdot \boldsymbol{\omega} \, \mathrm{d}V, \tag{2.1}$$

where $\boldsymbol{\omega} = \nabla \times \boldsymbol{u}$ and $V = V(\Omega)$ represents the volume of the vorticity region Ω. For quantum systems, we have

$$\mathcal{H} = \Gamma \oint_{\mathcal{C}} \boldsymbol{u} \cdot \mathrm{d}X = \Gamma \oint_{\mathcal{C}} \nabla\theta \cdot \mathrm{d}X = 0, \tag{2.2}$$

because vorticity is singular on $\mathcal{C}$ and the domain of vorticity has measure zero (in distributional sense). This zero helicity result can be obtained also by direct application of Noether's theorem (Kedia *et al.* 2018). When vorticity is localized on N thin filaments of centreline $\mathcal{C}_i$ ($i = 1, \ldots, N$), helicity admits topological interpretation in terms of linking numbers; in general, we have (Moffatt 1969; Moffatt & Ricca 1992; Ricca 1998)

$$\mathcal{H} = \sum_{i} \Gamma_i Sl_i + \sum_{i \neq j} \Gamma_i \Gamma_j Lk_{ij}, \tag{2.3}$$

where Sl_i is the Călugăreanu self-linking number, a topological invariant of the ith defect, and Lk_{ij} is the Gauss linking number, a topological invariant of the link between defects i and j, with $i \neq j$ ($i, j = 1, \ldots, N$). It is well known that $Sl_i = Wr_i + Tw_i$, where Wr_i denotes writhing number and Tw_i total twist (remember that total twist can be further decomposed into total torsion and intrinsic twist) (Moffatt & Ricca 1992). In the case of quantum fluids Salman (2017) showed that the topological interpretation of helicity given by (2.3) holds true also for condensates and can be applied to quantum defects. There is no difficulty to compute $Wr_i = Wr_i(\mathcal{C}_i)$ and $Lk_{ij} = Lk(\mathcal{C}_i, \mathcal{C}_j)$ for knots and links using

analytical definitions, or the algebraic interpretation in terms of apparent crossings (Ricca & Nipoti 2011). Computation of twist, however, requires the definition of a mathematical ribbon. A practical way to proceed is to take advantage of the foliation of the ambient space by the family of isophase surfaces S hinged on $\mathcal{C}_i$. The ribbon $\mathcal{R}_i$ can then be defined by taking the portion of Seifert surface determined by $\mathcal{C}_i$ (baseline of $\mathcal{R}_i$) and its push-off $\mathcal{C}_i'$ on S, congruently oriented with $\mathcal{C}_i$ and such that $Lk(\mathcal{C}_i, \mathcal{C}_i') = 0$. This gives a Seifert framing for $\mathcal{C}_i$ that is used for computation of $Tw_i = Tw_i(\mathcal{R}_i)$ (Zuccher & Ricca 2015). Note that Seifert framing is independent of the particular Seifert surface chosen for $\mathcal{C}_i$, and computation of Tw_i is independent of the choice of S.

If we denote by $\mathcal{L}$ the link given by a disjoint union (denoted by $\sqcup$) of $\mathcal{C}_i$, we have the following theorem (Sumners, Cruz-White & Ricca 2021).

THEOREM 2.1 (Zero helicity). *If $\mathcal{L} = \sqcup_i \mathcal{C}_i$ has Seifert framing then $\mathcal{H} = \mathcal{H}(\mathcal{C}_i) = 0$ for all $i = 1, \ldots, N$, and $\mathcal{H}(\mathcal{L}) = \sum_i \mathcal{H}(\mathcal{C}_i) = 0$.*

This result is confirmed by several numerical experiments (see, for example, Zuccher & Ricca 2017, hereafter referred to as ZR17). The zero helicity theorem provides topological conditions for the existence of potentially stable states. Since GPE defects have Seifert framing, total helicity is zero, so that total linking number must be zero; this means that when several defects are present, the sum of mutual linking and self-linking of individual components must be zero, putting consequentially constraints on the writhe and twist of each individual defect. An example of this has been tested by Zuccher & Ricca (2018), who considered the superposition of uniform twist $Tw = +1$ on an isolated, vortex ring with initially $Wr_1 = Tw_1 = 0$ ($Sl_1 = 0$ and $\mathcal{H} = 0$). Since the planar ring acquires new twist ($\Delta Tw_1 = +1$), then the jump $\Delta Sl_1 = +1$ triggers an instantaneous production of a secondary defect, linked with the first so that $Sl_1 = +1$, $Sl_2 = +1$ and $Lk_{12} = Lk_{21} = -1$, keeping $\mathcal{H} = 0$. A hydrodynamic interpretation and a topological proof of this is given by Foresti & Ricca (2019).

As mentioned previously, evolution of quantum defects is in many ways similar to that of Euler flows, because long-distance interaction is governed by the Biot–Savart law (Bustamante & Nazarenko 2015). Topology however is not conserved under GPE. Upon short-distance effects and interaction quantum defects can undergo topological changes by reconnection, similarly to what happens to classical vortex filaments in viscous flows. Several numerical experiments done on the evolution of knotted and linked defects (Proment, Onorato & Barenghi 2012; Clark di Leoni, Mininni & Brachet 2016; Kleckner *et al.* 2016; Zuccher & Ricca 2017; Bai, Yang & Liu 2020) show that often defects evolve and decay following what we may call a direct topological cascade through a stepwise unlinking sequence of topological simplifications. The topological decay has generic features dictated by reconnections that gradually reduce complex knots/links to small-scale unknotted, unlinked rings. Assuming that at any stage only a single reconnection event takes place, the whole process (exemplified by figure 1*a*–*f*) can be described by the following idealized sequence:

$$\ldots \to \mathcal{T}(2, 6) \to \mathcal{T}(2, 5) \to \ldots \to \mathcal{T}(2, 1) \to \mathcal{T}(2, 0). \tag{2.4}$$

Here $\mathcal{T}(p, q)$ denotes a generic knot/link type represented by a closed braid standardly embedded on a mathematical torus $\mathbb{T}$ (Oberti & Ricca 2016), where $p = 2$ denotes the number of wraps that the braid makes in the longitudinal (toroidal) direction, and q (integer) the number of wraps in the meridian (poloidal) direction. In this representation topological complexity is simply given by the crossing number $q \geq 2N$, and topological change by the reduction of q due to a single reconnection event (supposedly taking place
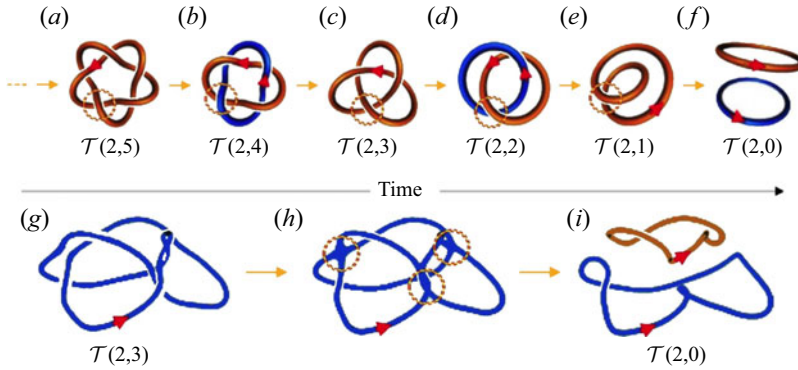
Figure 1. (*a–f*) Time sequence of topological cascade of idealized torus knots and links $\mathcal{T}(p, q)$: change of topology is due to a single reconnection event (not shown) supposedly occurring at a specific site exemplified by the encircled region. (*g–i*) Snapshots of numerical evolution of a trefoil knot defect governed by the Gross–Piteavskii equation: the knot $\mathcal{T}(2, 3)$ undergoes three simultaneous reconnections that create a system of two unlinked, unknotted loops $\mathcal{T}(2, 0)$. Bottom diagrams adapted from Proment *et al.* (2012). Red arrows on strands denote vorticity direction.

in the encircled region of figure 1*a–f*). The topological sequence (2.4) was observed in the unlinking pattern of DNA catenanes subject to site-specific enzyme recombinations (Shimokawa *et al.* 2013; Stolz *et al.* 2017), while the last stages of the sequence were observed experimentally in the evolution of a vortex trefoil knot in water (Kleckner & Irvine 2013) and in GPE simulations (see, for instance, Kleckner *et al.* (2016) and ZR17).

A more dramatic reduction of topological complexity occurs when multiple reconnections take place concurrently; if $n \leq q$ simultaneous reconnections occur, we have $\mathcal{T}(p, q) \rightarrow \mathcal{T}(p, q - n)$ with a drastic reduction of topology. Such a topological collapse can be achieved when the geometry of the interacting strands is highly symmetric, a rather improbable situation in nature, but easily achieved in numerical experiments. This can be obtained, for example, by superposing n helical wave perturbations on a vortex ring producing the decay of torus knots $\mathcal{T}(p, q)$ directly to a pair of convoluted rings $\mathcal{T}(2, 0)$ (see the example in figure 1*g–i*) (Proment *et al.* 2012; Bai *et al.* 2020). This topological collapse has been observed also in direct numerical simulations of a reconnecting trefoil knot under Navier–Stokes equations (Yao, Yang & Hussain 2021), where a much richer scenario due to vorticity diffusion shows the formation of bridges and threads of vorticity in the immediate aftermath of the reconnection stage.

These types of topological scenarios are not the only ones possible. Recent numerical simulations of superfluid turbulence have shown that rather complex knots may not only form during evolution (Mesgarnezhad *et al.* 2018), but they can interact and reconnect to create, temporarily, even more complex knots. Localized networks of vortex lines may undergo simultaneous reconnections to produce entanglements of much greater topological complexity. This inverse topological cascade, where topological complexity may momentarily increase rather than simplify, has been observed in numerical simulations of superfluid tangles, where 'monster knots' of incredibly high complexity can arise (Cooper *et al.* 2019).

In this case topological analysis must be based on descriptors more sophisticated than crossing numbers, such as Alexander, Jones and HOMFLYPT knot polynomials (Kauffman 2001). 'Monster knots' were indeed detected by Cooper *et al.* (2019) using the Alexander polynomial. Liu & Ricca (2012, 2015) derived Jones and HOMFLYPT

polynomials directly from helicity, proving that these are new topological invariants of ideal fluid mechanics that can be used to quantify topological changes and complexity. Direct application of these polynomials to the sequence (2.4), for example, showed that (2.4) can be put in one-to-one relation with a monotonically decreasing sequence of numerical values and energy contents (Liu & Ricca 2016).

Finally, let us remark that since reconnection of quantum knots preserve orientation, Seifert framing is also conserved. This means that according to the sequence (2.4) above, we can state the following theorem (Sumners *et al.* 2021).

THEOREM 2.2 (Zero helicity under topological cascade). *Consider the sequence (2.4):* $\mathcal{H}[\mathcal{T}(2,0)] = 0$ *if and only if* $\mathcal{H}[\mathcal{T}(2,q)] = 0$, *and any* $\mathcal{T}(2,q) = 0$ *has Seifert framing.*

Taking any two-component link of (2.4), let $\mathcal{L} = \mathcal{C}_1 \sqcup \mathcal{C}_2$ denote the disjoint union of Seifert framed defects $\mathcal{C}_1$ and $\mathcal{C}_2$, whose reference ribbons are given by $\mathcal{R}_1$ and $\mathcal{R}_2$, respectively; let $\mathcal{C}_1 \# \mathcal{C}_2$ be their reconnected sum, with ribbon $\mathcal{R}_1 \# \mathcal{R}_2$; then we have the following theorem.

THEOREM 2.3 (Total twist conservation). *The total twist of two Seifert framed defects* $\mathcal{C}_1$ *and* $\mathcal{C}_2$ *is conserved under anti-parallel reconnection, that is,* $Tw(\mathcal{R}_1) + Tw(\mathcal{R}_2) = Tw(\mathcal{R}_1 \# \mathcal{R}_2)$.

These theorems will be useful for the analysis of the results obtained by the test cases considered in § 4

3. Numerical methods

Before proceeding to consider various evolutionary scenarios we give some basic information on the numerical scheme. The dimensionless form of (1.1) (taking $\hbar/m = 1$) has coefficients of the Laplacian and nonlinear term equal to $1/2$; this implies that $\Gamma = 2\pi$, the healing length $\xi = 1$ and the Mach number (cf. equation (21) of Nore, Abid & Brachet 1997) $M = \sqrt{2}$; these values have been adopted in all simulations, and compressibility has been therefore taken into account.

Numerical solution to the three-dimensional GPE (1.1) is computed by employing a new technique recently proposed by Caliari & Zuccher (2021). The code exploits a mapping that rescales appropriately space variables, so that problems with boundary conditions are automatically resolved. We write $\boldsymbol{x} = (x_1, x_2, x_3)$ in terms of the new space variable $\boldsymbol{y} = (y_1, y_2, y_3)$; let

$$y_k(x_k) = \frac{2}{\pi} \arctan\left(\frac{x_k}{\alpha_k}\right) \quad (\alpha_k > 0; \; k = 1, 2, 3), \tag{3.1}$$

so that in each direction the unbounded space is mapped to the open interval $(-\infty, +\infty) \mapsto (-1, 1)$. Using (3.1) we have $\psi(\boldsymbol{x}, t) \mapsto \eta(\boldsymbol{y}, t)$, thus reducing the numerical search for solutions to a free-boundary approach. The governing equation (1.1) becomes

$$\eta_t = \frac{i}{2} \left[\sum_{k=1}^{3} \left(y_k'^2 \frac{\partial^2 \eta}{\partial y_k^2} + y_k'' \frac{\partial \eta}{\partial y_i} \right) + 1 - |\eta|^2 \eta \right], \tag{3.2}$$

where prime denotes space derivative. Space discretization is uniquely determined once the number of points n_k and scale factor α_k are prescribed. Each interval $(-1, 1)_k$ is

942 A8-6

discretized by n_k points $y_k^m = -1 + 2m/(n_k + 1)$, with $m = 1, 2, \ldots, n_k$ ($k = 1, 2, 3$). The Strang splitting method is chosen for time discretization; first and second space derivative operators are discretized by either fourth-order central finite differences or one-sided finite differences according to the number of neighbouring points available. The linear part of the equation is solved by a new and fast approximation of the action of the matrix exponential at machine precision accuracy (see Caliari & Zuccher 2021, for details), while the nonlinear part is solved exactly. Compared with the Fourier pseudo-spectral method used previously (see Zuccher *et al.* 2012), the present method not only outperforms the previous one in terms of CPU and memory usage, but it resolves the limits imposed by boundary conditions on a truncated domain, providing a much more reliable time evolution of integral quantities like mass, energy and momentum.

3.1. *Initial conditions: numerical details*

Numerically speaking the straight vortex line represents the only true, time-independent, exact solution to the GPE that can be used to check the numerical reliability of any GPE code (see Caliari & Zuccher 2018, and comments therein). All other types of vortex configuration, including vortex rings, knots and links require *ad hoc* techniques to generate initial conditions (see, for example, Proment *et al.* 2012; Clark di Leoni *et al.* 2016; Bai *et al.* 2020). Another common approach is to employ the Biot–Savart integral to compute the induced velocity field $\boldsymbol{u} = \boldsymbol{\nabla}\theta$, extracting the phase $\theta(\boldsymbol{x})$ by direct integration (see, for example, Scheeler *et al.* 2014). This method, however, gives rise to numerical problems when integration is very close to the nodal line where phase is ill-defined. To overcome this difficulty, we adopt a different approach: we set $\theta = 0$ at a point (in the computational domain) sufficiently distant from a defect line and integrate along paths that start from that point and go either towards infinity or terminate on the defect line. The difficulty associated with an undefined phase is thus resolved. Once the initial phase is computed, we follow the standard technique to prescribe density evaluated at each grid point by the minimum distance from the closest nodal line according to the fourth-order Padé approximation of the straight vortex solution.

As an initial condition, we use either the self-preserving quantum ring solution (Zuccher & Caliari 2021), or some prescribed parametric equations of nodal lines according to the technique discussed above. Several initial geometries and topologies will be considered in § 4: the Hopf link (referred to as HOPF), the head-on collision of two perturbed rings (HOC), several torus knots (in particular the $\mathcal{T}(2, 9)$, referred to as T29), the collision of three rings (3R), the interaction of two elliptical rings (2E) and the interaction of two perturbed rings (2P). Perturbation of a ring is given by

$$\boldsymbol{X} : \begin{cases} X(t) = [R + A_i \cos(mt)] \cos t, \\ Y(t) = [R + A_i \cos(mt)] \sin t, \\ Z(t) = A_o \cos\left[m\left(t - \dfrac{\pi}{6}\right)\right], \end{cases} \tag{3.3}$$

where R is the radius of the unperturbed ring, A_i the perturbation of the components in the xy-plane, A_o the perturbation of the out-of-plane component and m the wavenumber. Torus knots $\mathcal{T}(p, q)$ are given by

$$\boldsymbol{X} : \begin{cases} X(t) = \left[R + r \cos(qt)\right] \cos(pt), \\ Y(t) = \left[R + r \cos(qt)\right] \sin(pt), \\ Z(t) = r \sin(qt), \end{cases} \tag{3.4}$$

Case	$N_x \times N_y \times N_z$	$\alpha_1, \alpha_2, \alpha_3$	Physical domain	Δt	Initial condition
HOPF	$171 \times 171 \times 171$	15, 15, 15	$[-821, 821]^3$	0.02	ZR
HOC	$187 \times 187 \times 187$	15, 15, 15	$[-898, 898]^3$	0.02	BS
T29	$171 \times 171 \times 171$	15, 15, 15	$[-821, 821]^3$	0.02	BS
3R	$171 \times 171 \times 171$	15, 15, 15	$[-821, 821]^3$	0.02	SP
2E	$171 \times 171 \times 171$	15, 15, 15	$[-821, 821]^3$	0.02	BS
2P	$171 \times 171 \times 171$	15, 15, 15	$[-821, 821]^3$	0.02	BS

Table 1. Case considered, degrees of freedom $N_x \times N_y \times N_z$, α_k-values ($k = 1, 2, 3$), physical domain, time step Δt and type of initial condition: ZR, rings generated as in ZR17; BS, Biot–Savart generation; SP, self-preserving rings generated by the product of initial conditions ψ_{0v} ($v = 1, 2, 3$) for each of the three self-preserving rings (according to Zuccher & Caliari 2021).

where R and r are respectively the large and small radius of the torus $\mathbb{T}$, p and q are the number of wraps along the longitudinal and meridian direction of $\mathbb{T}$.

Details of the initial conditions used in the simulations are summarized here below.

Case H3L: the case discussed in ZR17 is repeated with the new code; 2 rings of radius $R = 8$ are placed on mutually orthogonal planes, one centred at $(0.5, 4.5, 0)$ moving in the positive direction of x_3 ($\equiv z$), the other centred at $(0, -4, 0)$ moving in the positive direction of x_1 ($\equiv x$).

Case HOC: two rings of radius $R = 17.4$ perturbed according to (3.3), with $A_i = 0.8$, $A_o = 0.22$ and wavenumber $m = 11$, are placed in two parallel planes $x = \pm 4$ mirror imaging one another.

Case T29: knot $\mathcal{T}(2, 9)$ given by (3.4), with $R = 10$, $r = 3.3$, $p = 2$ and $q = 9$, placed at the origin.

Case 3R: three self-preserving rings with radius $R = 8$; first ring centred at $(-12, -4, 0)$ moving in the positive direction of x_1 ($\equiv x$), second ring centred at $(0, -12, -6)$ moving in the positive direction of x_2 ($\equiv y$), third ring centred at $(0.5, 4.5, -12)$ moving in the positive direction of x_3 ($\equiv z$).

Case 2E: two ellipses given in parametric form by $(a \cos t, b \sin t)$; first ellipse of semi-axes $a = 5$ and $b = 12$ centred at the origin; second ellipse of semi-axes $a = 4$ and $b = 12$ centred at $(0, 0, -3)$ and rotated by $\pi/4$ with respect to the first.

Case 2P: two rings of radius $R = 10$, perturbed according to (3.3) with $A_i = 2$, $A_o = 1$ and wavenumber $m = 3$; first ring centred at the origin, second ring centred at $(1, 0, -4)$ and rotated by $\pi/3$ with respect to the first.

The numerical details of the simulations are shown in table 1.

3.2. *Evaluation of geometric and topological properties*

Nodal lines are identified following the same procedure used in previous works (see, for example, ZR17). We first spline interpolate ψ on a very fine grid and look for points where $\rho = |\psi|^2 \to 0$. Scattered points are then organized to form closed, smooth loops oriented according to vorticity direction. Total length L (non-dimensionalized by the healing length ξ) and total curvature K (pure number) are defined considering the number $i = 1, \ldots, N$

of nodal lines present, according to

$$L = \sum_{i=1}^{N} \oint_{C_i} ds, \quad K = \frac{1}{2\pi} \left[\sum_{i=1}^{N} \oint_{C_i} c(s) \, ds \right], \tag{3.5a,b}$$

where $c(s)$ is local curvature (function of arc length s of each nodal line C_i); this requires a continuous second derivative of the vector position $X = X(s)$. Other quantities such as total writhing number $Wr_i = Wr(C_i)$ and linking number $Lk_{ij} = Lk(C_i, C_j)$ are computed by their integral definition (Moffatt & Ricca 1992) using information on the nodal line identification. We have

$$Wr_i = \frac{1}{4\pi} \oint_{C_i} \oint_{C_i} \frac{(X_i - X_i^*) \cdot dX_i \times dX_i^*}{|X_i - X_i^*|^3}, \tag{3.6}$$

where X_i and X_i^* denote two distinct points on C_i; remember that writhe is a global geometric property of a space curve that takes real values, and it is zero for plane curves. We also have

$$Lk_{ij} = \frac{1}{4\pi} \oint_{C_i} \oint_{C_j} \frac{(X_i - X_j) \cdot dX_i \times dX_j}{|X_i - X_j|^3}, \tag{3.7}$$

where $X_i \in C_i$ and $X_j \in C_j$; Lk_{ij} takes only integer values. As for the computation of the total twist number $Tw_i = Tw(\mathcal{R}_i)$, we follow the procedure introduced by Zuccher & Ricca (2015) through the identification of the ribbon $\mathcal{R}_i$ by the unit vector $\hat{U} = \hat{U}(s)$ on each C_i; we have

$$Tw_i = \frac{1}{2\pi} \oint_{C_i} \left(\hat{U} \times \frac{d\hat{U}}{ds} \right) \cdot \hat{T} \, ds. \tag{3.8}$$

This integral, which takes real values, is also a global geometric property of C_i through its ribbon. Since the ambient space is foliated by infinitely many isophase surfaces hinged on C_i, twist computation is independent from the choice of a specific isophase surface.

3.3. *Evaluation of isophase surfaces and energy integrals*

Computation of isophase surface areas is carried out by one of the many numerical codes available in the literature using standard triangulation techniques. For a given value of the phase θ, the area $A = A(S_\theta)$ of the isophase surface is given by

$$A(S_\theta) = \sum_{\nu} A_\nu = \sum_{\nu} \frac{1}{2} \|V_{\nu 1} \times V_{\nu 2}\|, \tag{3.9}$$

where $V_{\nu 1}$ and $V_{\nu 2}$ denote the two edges (in vector form) of the νth triangle. At a fixed simulation time $A(S_\theta)$ reaches a global minimum $A_{min} = A(S_{min})$ for $\theta = \theta_{min}$; by repeating this search at each simulation time we get $A_{min} = A_{min}(t)$ (see § 6 below).

Another quantity associated with the evolution of S is the energy $\mathcal{E}(S)$ computed as a surface integral of a certain energy density e (energy per unit volume). From a numerical viewpoint we interpolate the energy density at the centre of gravity G_ν of each face F_ν of S to get e_ν. Denoting by $\mathcal{E}(S)$ the integral of e over S (thus getting an energy per unit length) and by $\bar{\mathcal{E}}(S)$ the average value, we have

$$\mathcal{E}(S) = \int_S e \, dS = \sum_{\nu} e_\nu A_\nu, \quad \bar{\mathcal{E}}(S) = \frac{\mathcal{E}(S)}{A(S)} = \frac{\sum_{\nu} e_\nu A_\nu}{\sum_{\nu} A_\nu}. \tag{3.10a,b}$$

(*a*)   (*b*)   (*c*)
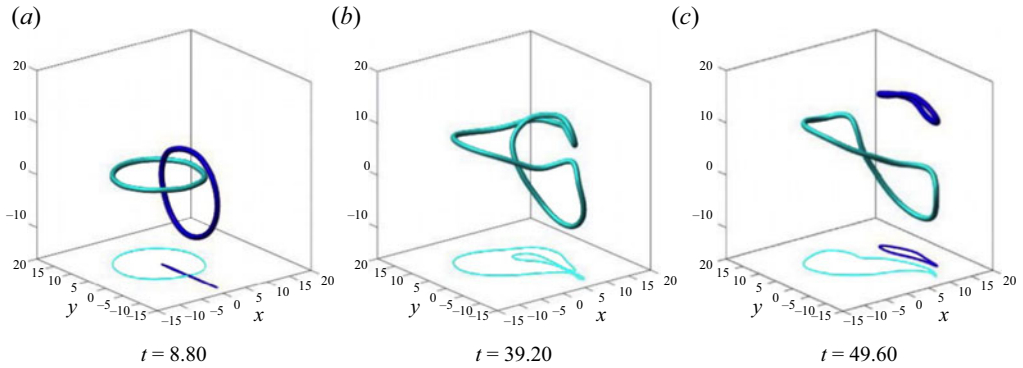

$t = 8.80$ $t = 39.20$ $t = 49.60$

Figure 2. The HOPF case; snapshots of topological cascade of Hopf link to a pair of unlinked, unknotted loops: link $\mathcal{T}(2, 2) \rightarrow 1$ loop $\rightarrow 2$ loops $\mathcal{T}(2, 0)$; single reconnection events at time $t = 38.00$ and $t = 42.40$ (reconnection stages not shown).

4. Creation and evolution of quantum knots and links

The evolutionary scenarios identified in §2 are here investigated by the test cases mentioned in the previous section.

4.1. *Direct topological cascade and collapse*

A simple example of direct topological cascade is given by the evolution of the Hopf link $\mathcal{T}(2, 2)$ (HOPF case) shown in figure 2. Results obtained by the new code confirm what was found by previous simulations (Clark di Leoni *et al.* 2016; Kleckner *et al.* 2016; Salman 2017; Zuccher & Ricca 2017; Villois, Proment & Krstulovich 2020). The link undergoes a first reconnection to form a single unlinked, unknotted loop $\mathcal{T}(2, 1)$ that reconnects again to form two separate small loops $\mathcal{T}(2, 0)$. The pattern found for the decay process of a trefoil knot follows the sequence (2.4). Interaction and topological decay of more complex systems given by linked, vortex tangles were observed by Villois, Proment & Krstulovic (2016) with the production of separated, unlinked loops. Another interesting example is provided by the topological collapse given by the head-on collision of two vortex rings (HOC case). This is the quantum version of the famous experiment of two vortex rings in water by Lim & Nickels (1992). According to the initial conditions described in §3.1, the two perturbed rings are seen to approach each other and stretch (figure 3). When they are in close proximity, the mirror symmetric perturbations give rise to 11 simultaneous reconnection events, equi-spaced all along the reconnection circular region centred on the mutual axis of propagation; as a result, 11 small vortex rings are created all around the collisional axis, propagating radially away from the reconnection region (see Movie 1 in supplementary material available at https://doi.org/10.1017/jfm. 2022.362). Since in quantum hydrodynamics circulation is strictly constant, we cannot have diffusive fragmentation of nodal lines; hence, threads and bridges of weaker vorticity visible in viscous flows (as shown by Cheng, Lou & Lim 2018) cannot be reproduced here, but the key features of the process are nevertheless well captured by the quantum code.

Other examples of topological collapse are given by considering the evolution of perfectly symmetric torus knots. To show this, let us consider the evolution of $\mathcal{T}(2, 9)$ (shown in figure 4 and referred to as T29). By symmetry the nine helical coils of the knot produce nine simultaneous reconnections. As a result, the knot type $\mathcal{T}(2, 9)$ jumps directly to $\mathcal{T}(2, 0)$ creating two separate loops: the leading ring (dark blue in figure 4) and
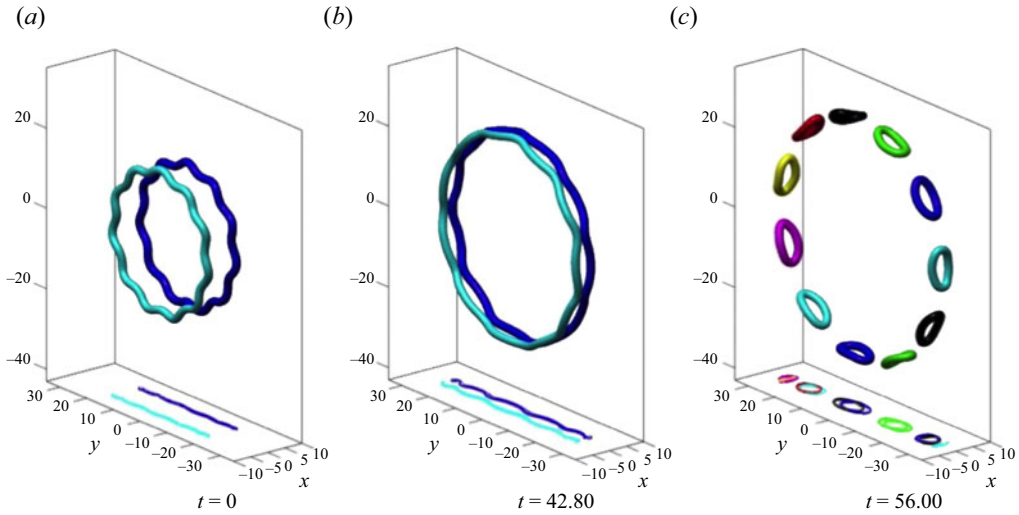
Figure 3. The HOC case; snapshots of topological collapse due to the head-on collision of two vortex rings: 2 large rings → 11 small rings; 11 simultaneous reconnection events at time $t = 46.80$ (reconnection stage not shown).
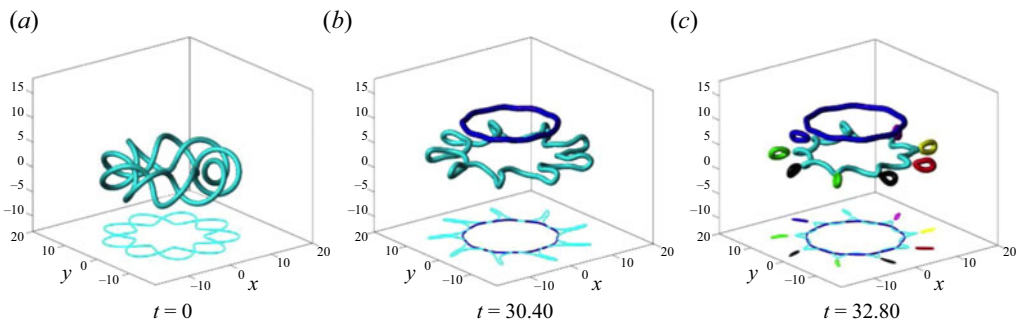

Figure 4. Case T29; snapshots of topological collapse of torus knot: $\mathcal{T}(2, 9) \rightarrow$ two loops → two loops and nine small rings; nine simultaneous reconnection events at time $t = 16.00$ followed by other nine simultaneous reconnections at $t = 32.40$ (reconnection stages not shown).

a convoluted trailing loop behind. The coiled regions of the trailing loop trigger then other nine simultaneous reconnections creating nine small vortex rings. In this case the cascade process is realized by the topological collapse of a large, single structure to produce first a medium sized, and then small-scale structures (see Movie 2 available as supplementary material).

4.2. *Structural and topological cycles*

Cases of structural and topological cycles may occur frequently. A structural cyclic process is represented by the creation of a number of disconnected components, whose total length may temporarily increase before further decay. One simple example (case 3R) is represented by the '3-2-1-2-3' cycle of figure 5, where collision of three rings propagating one against the others in mutually orthogonal planes brings first the creation of two loops, then one long loop before decaying to form two loops, and then three loops of
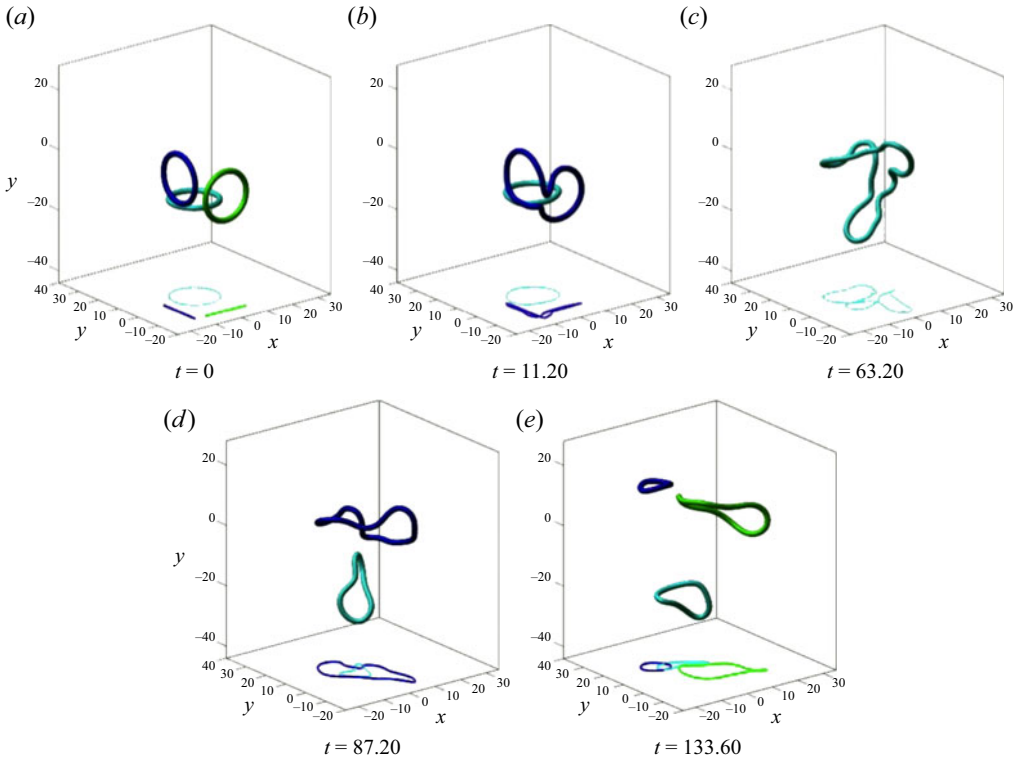
Figure 5. Case 3R; snapshots of structural cycle of three mutually perpendicular rings: three loops → two loops → one loop → two loops → three loops; single reconnection events at time $t = 9.20$, $t = 20.40$, $t = 84.00$, $t = 116.40$ (reconnection stages not shown).

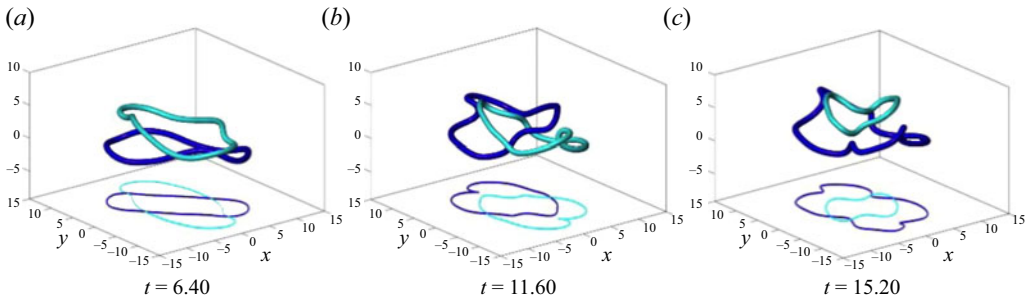Figure 6. Case 2E; creation of Hopf link from two planar ellipses: two unlinked loops → Hopf link $\mathcal{T}(2, 2)$ → two unlinked loops; single reconnection event at time $t = 11.00$ followed by two simultaneous reconnections at $t = 14.40$ (reconnection stages not shown).

shorter length. The whole process is governed by a sequence of single reconnection events. Similarly for the topological cycle shown in figure 6 (case 2E) represented by the sequence $\mathcal{T}(2, 0) \rightarrow \mathcal{T}(2, 1) \rightarrow \mathcal{T}(2, 0)$, where the temporary increase of topology due to the creation of a Hopf link gives way to the production of two unlinked, unknotted loops.

942 A8-12

(*a*) (*b*) (*c*) (*d*)

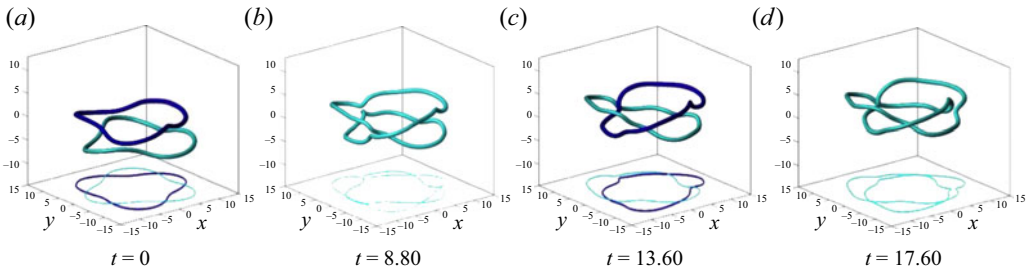$t = 0$ $t = 8.80$ $t = 13.60$ $t = 17.60$

Figure 7. Case 2P; creation of trefoil knot from two unlinked, perturbed rings: two loops $\mathcal{T}(2, 0) \rightarrow$ one loop $\mathcal{T}(2, 1) \rightarrow$ Hopf link $\mathcal{T}(2, 2) \rightarrow$ trefoil knot $\mathcal{T}(2, 3)$; single reconnection events at $t = 7.60$, $t = 11.20$, $t = 16.80$ (reconnection stages not shown).

4.3. *Inverse topological cascade: creation of trefoil knot*

As mentioned in § 2, inverse topological cascades characterized by the evolution of topologically simple structures to produce more complex ones are also possible. In figure 7 we show an example of such a phenomenon (case 2P), where two initially disjoint, unknotted and unlinked perturbed rings interact to create first a single convoluted loop, then a Hopf link, and finally a trefoil knot. Note that this remarkable sequence reproduces in reverse order the sequence (2.4) above (see Movie 3 available as supplementary material). This production of the trefoil knot by GPE shows how topologically non-trivial knots can indeed be created from topologically unlinked, unknotted loops, similarly to what was done by Villois *et al.* (2016). The present experiment, first conjectured a long time ago by one of the current authors (see Ricca 2009, figure 1 and discussion of the proposed experiment therein), shows how crucial the role of the initial conditions is to determine topologically complex configurations. Contrary to the experiment done by Kleckner & Irvine (2013), where topology of the vorticity field is transferred from the initial, existing topology of the trefoil shaped airfoil to the pressure field, here new topology is created from truly trivial initial conditions.

5. Length rate of change, curvature and writhe as dynamical markers

5.1. *Total length and total curvature*

Total length L and total curvature K are computed for all the cases discussed above; results are shown in figure 8 only for the cases T29 (topological collapse), 3R (structural cycle), 2E (topological cycle) and 2P (inverse topological cascade). For the case of the Hopf link evolution (direct topological cascade) shown in figure 2, the interested reader can refer to the results published in ZR17.

Total length (denoted by red squares in plots of figure 8, scale on the right) gets generically stretched as defect lines get closer. This is consistent with the classical scenarios observed for vortex filaments (Siggia 1985; Kerr 2011), and it is due to the induction effect of the Biot–Savart law. As pointed out by Villois *et al.* (2020), the rate of change $\delta L/\delta t$ appears to be markedly higher (in absolute value) in the post-reconnection stage rather than during pre-reconnection. The consequent faster separation time of defects, due to the higher speed of the separated strands, is given by the higher curvature of the recombined strands immediately after reconnection. This is further confirmation of the time asymmetry and irreversibility of the process due to sound emission during reconnection, which is known to be responsible for the energy loss, as originally noticed by Leadbeater *et al.* (2001), and later confirmed by Zuccher *et al.* (2012) and
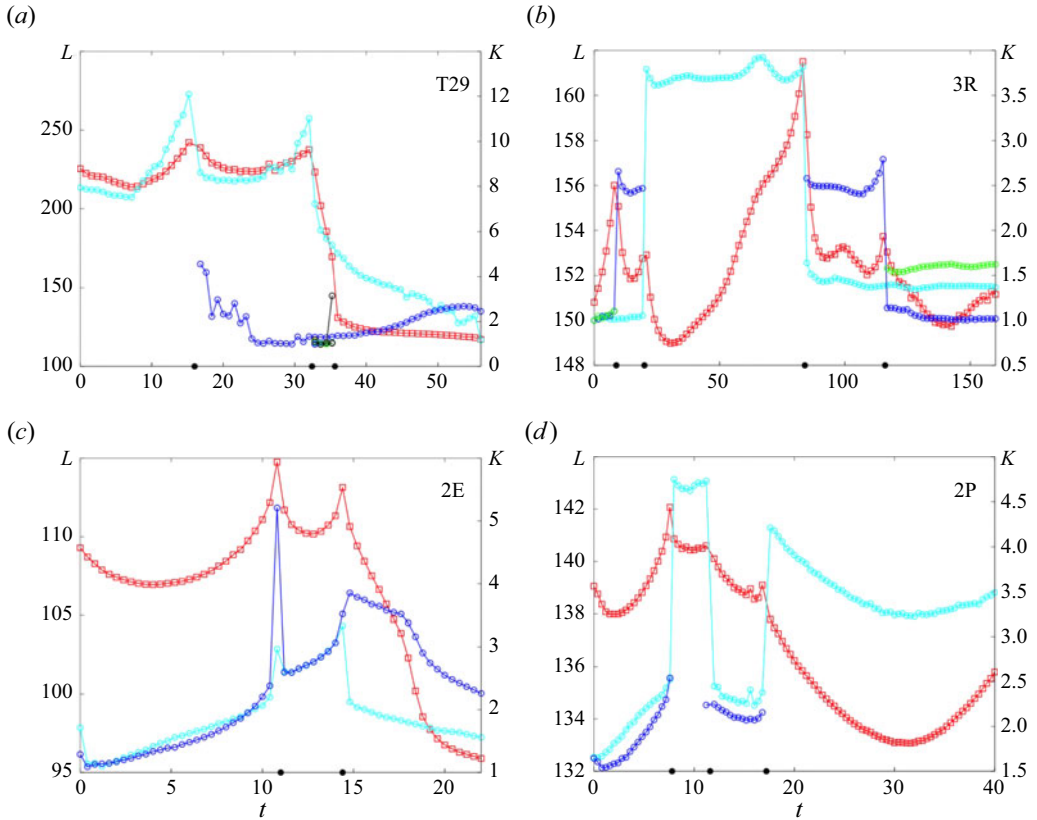
Figure 8. Total length L (red squares, scale on the left) and normalized total curvature K (circles of various colours, scale on the right) plotted against time t for T29, 3R, 2E, 2P. Circles of different colour identify different components created during evolution; black dots on time axis denote reconnection events.

Allen *et al.* (2014). This feature is well captured by plots of total curvature, where the pronounced picks and drops of K (figure 8, coloured circles) mark accurately the occurrence of reconnection events (denoted by black dots on the time axis).

5.2. *Writhe, total twist and helicity*

Plots of writhe, twist and total helicity for T29, 3R, 2E, 2P are shown in figure 9. In agreement with the results of theorems 2.1 and 2.2, total helicity (computed by (2.3) and denoted by red squares in the plots) remains zero at all times, involving a continuous exchange between writhe and twist during evolution. If writhe is essentially a sign of non-planarity, production of twist (intrinsic twist, in particular) gives rise to an axial flow of particles along the defect. The hydrodynamic interpretation of twist in terms of azimuthal and longitudinal velocity on classical vortex filaments has been numerically observed by Zuccher & Ricca (2018) and discussed in detail by Foresti & Ricca (2019). Crude estimates and instability analysis (Foresti & Ricca 2020) show that twist gradients along the nodal line may have an important role in defect dynamics, but in these simulations no specific bounds on twist values have been observed or imposed, other than noting total twist conservation across reconnections (in agreement with theorem 2.3). The apparently unbalanced jumps in 2E and 2P are due to the creation of the Hopf
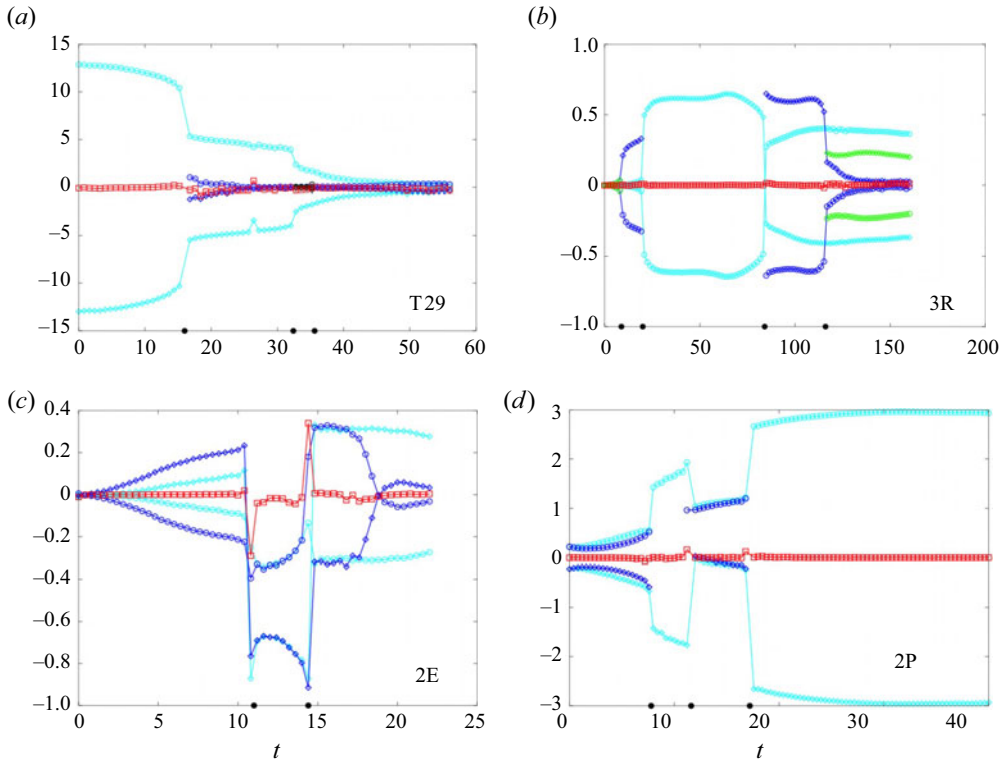
Figure 9. Writhe *Wr* (circles of various colours), total twist *Tw* (diamonds of various colours) and total helicity $\mathcal{H}$ (red squares) plotted against time *t* for T29, 3R, 2E, 2P. Circles and diamonds of different colour identify different components created during evolution; black dots on time axis denote reconnection events.

link and the consequential change in linking number $|\Delta Lk_{12}| = 1$. Direct topological cascade visualized by the Hopf link evolution (HOPF) or collapse (exemplified by HOC and T29) is detected by the decrease in writhe as a measure of the progressive decay towards unlinked, unknotted planar rings. Of course this behaviour is partially reversed under cyclic phenomena (as for 3R and 2E), or completely reversed in the presence of inverse cascade (see 2P).

6. Defect dynamics driven by minimal surfaces

6.1. *Energy contribution on isophase surface*

It is interesting to evaluate time dependence of energy contribution on an isophase surface. One such surface associated with the Hopf link evolution is shown in figure 10(*a*). The non-dimensional form of total energy E_{tot}, constant under GPE, is given by (Nore *et al.* 1997; Barenghi & Parker 2016)

$$E_{tot} = \int \left(\frac{1}{2} |\nabla \psi|^2 - \frac{1}{2} |\psi|^2 + \frac{1}{4} |\psi|^4 \right) dV. \tag{6.1}$$

By using Madelung's transformation we have

$$|\nabla \psi|^2 = \rho |\nabla \theta|^2 + \frac{|\nabla \rho|^2}{4\rho} = \rho |\boldsymbol{u}|^2 + \frac{|\nabla \rho|^2}{4\rho}; \tag{6.2}$$
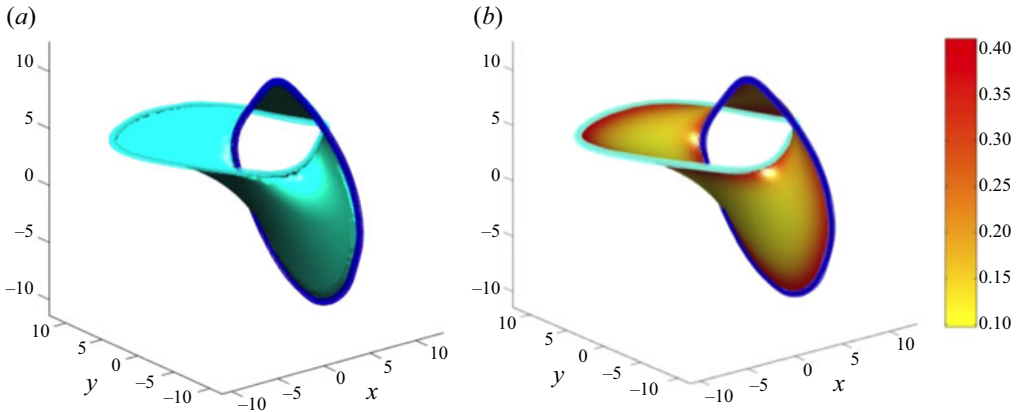
942 A8-15

Figure 10. The HOPF case; (*a*) isophase surface of least area (S_{min}) at $t = 23.20$; (*b*) same surface colour-coded by the sum $e_k + e_q$ (according to (3.10*a,b*) and (6.3)).

hence,

$$E_{tot} = \underbrace{\frac{1}{2} \int \rho |\boldsymbol{u}|^2 \, \mathrm{d}V}_{E_k} + \underbrace{\frac{1}{8} \int \frac{|\boldsymbol{\nabla}\rho|^2}{\rho} \, \mathrm{d}V}_{E_q} - \underbrace{\frac{1}{2} \int \rho \, \mathrm{d}V}_{E_p} + \underbrace{\frac{1}{4} \int \rho^2 \, \mathrm{d}V}_{E_i}, \qquad (6.3)$$

where E_k refers to kinetic energy, E_q quantum, E_p potential and E_i interaction (or internal) energy. Density reaches a constant value outside the healing region $O(\xi)$, and it decays rapidly to zero inside the healing region given by the tubular neighbourhood of $\mathcal{C}$ (Berloff 2004). This means that contributions from potential and interaction energy can be taken to be constant everywhere outside the healing regions and can be ignored in the bulk of the system. Direct computation of all these contributions on specific isophase surfaces (not shown) are made for comparison; the contribution from the sum of kinetic and quantum energy density is shown in figure 10(*b*).

6.2. *Minimal surface as critical energy surface*

Information on energy contributions is used to investigate the role of isophase surfaces $S = S_{min}$ of least geometric area and relation with energy and defect dynamics. As mentioned at the beginning of § 3, since the Mach number $M = \sqrt{2}$, compressibility is duly taken into account. However, since M is constant, its value cannot be used as an indicator of the importance of local compressible effects; to by-pass this problem, we look for the regions where density gradients are important by measuring quantum energy E_q, i.e. the contribution of compressibility to total energy (see (6.3)). To understand the implications of this, let us consider an isophase surface of least area (see figure 10*a*) and suppose to ignore the portions of such a surface where density gradients are relevant (that is, in the healing region). Let us denote by S'_{min} the portion of S_{min} bounded by $\mathcal{C}'_i$, i.e. where density is almost constant. From computational data (see the example of figure 10*b*) we see that the geometric contribution of this excluded area (where compressibility is important) is negligible compared with the total area of S_{min}, hence, the area of the minimal isophase surface S'_{min} where ρ is almost constant can be taken approximately
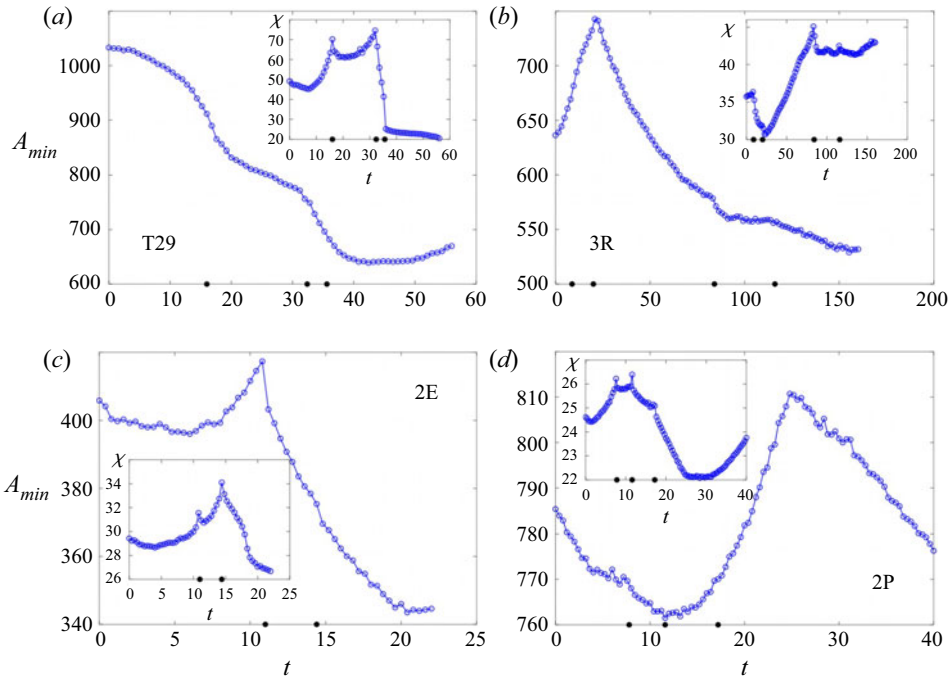
Figure 11. Evolution of (total) minimal area $A_{min} = A(S_{min})$ of isophase surface plotted against time for T29, 3R, 2E, 2P. Insets show time evolution of $\chi = L^2/A_{min}$. Black dots on time axis denote reconnection events.

equal to $A_{min} = A(S_{min})$. Since $\boldsymbol{u} = \boldsymbol{\nabla}\theta$, we have

$$\boldsymbol{\nabla} \cdot \boldsymbol{u} = 0 \;\Rightarrow\; \nabla^2\theta = 0 \quad \forall \boldsymbol{x} \in S'_{min}. \tag{6.4}$$

This shows that S'_{min} is harmonic and, being a conformal immersion in $\mathbb{R}^3$, it is critical with respect to the Dirichlet functional (Courant 1950)

$$D(\Theta) = \frac{1}{2}\int_{S'_{min}} |\boldsymbol{\nabla}\Theta|^2 \,\mathrm{d}S. \tag{6.5}$$

Minimal isophase surfaces are therefore expected to be privileged markers for energy, because

$$D(\Theta) \approx D(\psi)|_{S_{min}} = \frac{1}{2}\int_{S_{min}} |\boldsymbol{\nabla}\psi|^2 \,\mathrm{d}S. \tag{6.6}$$

By (6.2) and by recalling the definitions given by (3.10a,b), we have

$$D(\psi)|_{S_{min}} = \frac{1}{2}\int_{S_{min}} \left[\rho|\boldsymbol{u}|^2 + \frac{|\boldsymbol{\nabla}\rho|^2}{4\rho}\right] \mathrm{d}S = \int_{S_{min}} (e_k + e_q)\,\mathrm{d}S = \mathcal{E}_k + \mathcal{E}_q. \tag{6.7}$$

Relying on the result of theorem 2.2, which ensures that at each evolutionary state Seifert framing allows us to identify a minimal isophase surface, we proceed to compute S_{min}. The search for minimal surfaces associated with defect dynamics proves to be a rather demanding computational task. This is because of the large amount of information to be analysed at each instant of time and the computational difficulties associated with possibly highly convoluted geometry. Indeed, at each instant of time we must determine S_{min} by
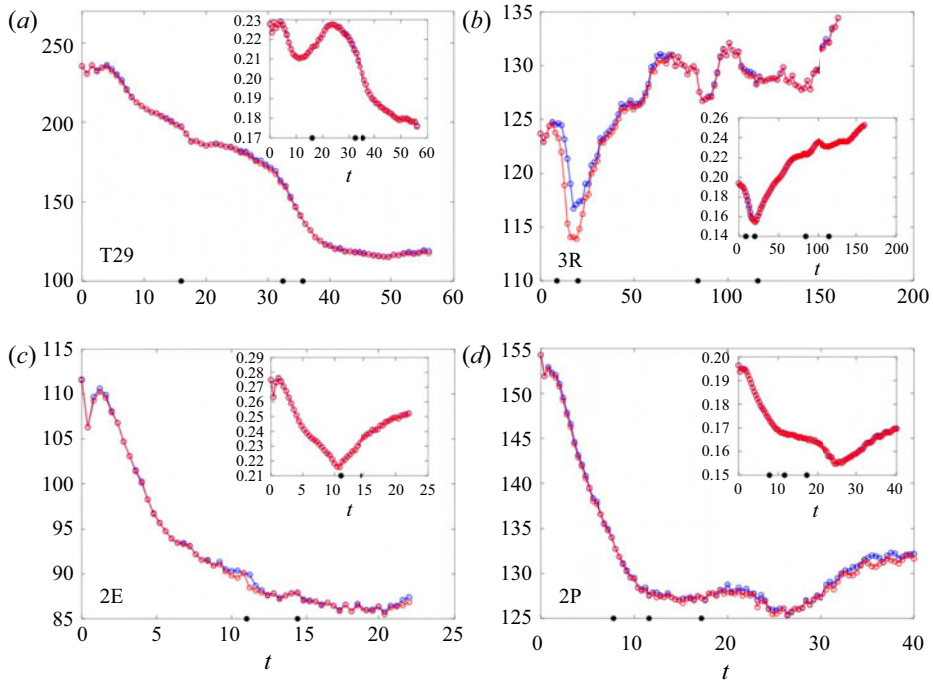
Figure 12. Time evolution of the maximal energy $\text{Max}[D(\psi)]$ (blue circles), computed instantaneously over all surfaces S for $\theta \in [0, 2\pi)$, and of $D(\psi)|_{S_{min}}$ (red circles), computed on $S = S_{min}$. Insets show time evolution of average values given by $\text{Max}[\bar{\mathcal{E}}_{kq}(S)]$ (blue circles) and $\bar{\mathcal{E}}_{kq}|_{S_{min}}$ (red circles). Black dots on time axis denote reconnection events.

selecting out of all possible values of $\theta \in [0, 2\pi)$ the surface of least geometric area given by measuring $A(S_{min}) = A_{min}$. This task is then repeated for all computational times.

Plots of $A_{min} = A_{min}(t)$ for T29, 3R, 2E, 2P are shown in figure 11. For the direct topological cascade of the Hopf link and torus knots $\mathcal{T}(2, 3)$, $\mathcal{T}(2, 5)$, $\mathcal{T}(2, 7)$ (not shown) as well as for the topological collapse exemplified by T29 (shown), we observe an almost monotonic decrease of A_{min}. The decrease of A_{min} is markedly uniform for the simplest knots tested (not shown), while for T29 A_{min}, starts to increase (as shown in figure) after the formation of small rings (when $t > 40$): this slight increase in slope is probably related to a highly convoluted surface geometry. For structural cycles, exemplified by the case 3R, A_{min} reaches a maximum when interaction between several components leads to a single defect line (third plot of figure 5), and after a second reconnection (at $t = 20.40$) A_{min} regain monotonic decrease towards small rings. The same behaviour is observed for 2E after creation of the Hopf link; consistently, for the inverse cascade (case 2P), we observe an increase of A_{min}, where the pick at $t \approx 27$ is probably due to a rather complicated geometry. Since for planar rings the ratio $\chi = L^2/A$ is minimum at $\chi = (2\pi R)^2/(\pi R^2) = 4\pi$, the monotonic areal decrease of S_{min} towards small, planar rings measured by writhe nullification of the Hopf link (as shown in ZR17, and visible in figure 8 for the case T29) demonstrates that evolutionary decay processes are indeed minimal surface energy relaxation processes. Plots of $\chi = \chi(t)$ (figure 11, insets) provide further confirmation of this.

The rate of change $\delta A_{min}/\delta t$ helps to discriminate processes that are energetically more favoured than others. The correlation between stationary points where $\mathrm{d}A_{min}(t)/\mathrm{d}t = 0$

and the presence of reconnection events (denoted by black dots on time axis) is evidence that changes of topology are invariably accompanied by critical rates of change of A_{min} and energy.

To make sure that S_{min} has physical relevance, we compute the average value of the sum of kinetic and quantum energy density, given by $\bar{\mathcal{E}}_{kq} = \bar{\mathcal{E}}_k + \bar{\mathcal{E}}_q$ (see again (3.10a,b) for definitions). We compare the maximal average value $\text{Max}[\bar{\mathcal{E}}_{kq}(S)]$ as S changes with $\theta \in [0, 2\pi)$ and $\bar{\mathcal{E}}_{kq}|_{S_{min}}$, i.e. the value of $\bar{\mathcal{E}}_{kq}$ computed on the isosurface of least area S_{min}. Plots of these data coincide almost everywhere for all the cases investigated, confirming that S_{min} is indeed critical for energy, and proves to be an appropriate marker for dynamics. As a further check, we compute also the integral quantities $\text{Max}[D(\psi)] \equiv \text{Max}[\mathcal{E}_k + \mathcal{E}_q]$, obtained by evaluating the maximum value of $D(\psi)$ over all surfaces for $\theta \in [0, 2\pi)$, and $D(\psi)|_{S_{min}}$. Direct comparison between $\text{Max}[D(\psi)]$ and $D(\psi)|_{S_{min}}$ shows that numerical values overlap almost everywhere. Figure 12 summarizes information on energy contents. Large plots show the time evolution of the maximum value $\text{Max}[D(\psi)]$ (blue circles) obtained instantaneously by evaluating maximum values over all surfaces for $\theta \in [0, 2\pi)$, and $D(\psi)|_{S_{min}}$ (red circles) computed instantaneously on $S = S_{min}$. Plots in insets show the average values given by $\text{Max}[\bar{\mathcal{E}}_{kq}(S)]$ (blue circles) and $\bar{\mathcal{E}}_{kq}|_{S_{min}}$ (red circles), where correlation between minimal surface energy relaxation and direct topological cascade for the case T29 and 2E after the Hopf link creation (at $t = 11$) is quite evident.

7. Conclusions

In this paper we have investigated geometric, topological end energy aspects of quantum vortex knots and links under the standard GPE. The constraints posed by quantum systems on defect localization and circulation make quantum hydrodynamics an ideal setting to apply geometric and topological techniques to get physical insight on evolutionary processes. In §2 we have identified three types of possible scenarios that characterize vortex knots interaction and evolution: direct cascade and collapse of topologically complex structures; structural and topological cycles from simple to complex to simple structures; inverse cascade, where topology may momentarily increase during evolution. These three scenarios have been investigated by direct numerical simulations of the governing equation based on a new numerical code that resolves the limits imposed by boundary conditions on a truncated domain (§3). Several test cases have been analysed in §4: as an example of direct topological cascade, we have reconsidered the evolution of a Hopf link (previously investigated using an earlier code in ZR17), and explored examples of topological collapse considering the head-on collision of quantum vortex rings by reproducing the famous experiment of Lim & Nickels (1992), and the direct decay of torus knot $\mathcal{T}(2, 9)$ (case T29). As an example of a structural cycle, we have investigated the interaction and evolution of three colliding vortex rings (case 3R), and a topological cycle has been realized through the creation and decay of a Hopf link starting from two unlinked, unknotted elliptical rings (case 2E). Finally, we have provided an example of inverse topological cascade by the creation, for the first time ever, of a trefoil knot starting from the interaction of two unlinked, unknotted loops (case 2P).

Results on the evolution of total length, curvature, writhe, twist and helicity are presented in §5. As originally noted by Zuccher *et al.* (2012), we confirm that the length rate of change, faster after reconnection due to the newly formed strands, breaks the time symmetry of GPE, a clear sign of irreversibility. This is also consistent with the observed marked picks of total curvature, as shown in plots of figure 8. Since defects admit Seifert framing through foliation of the ambient space by their isophase surfaces, the zero

helicity theorem 2.1 is confirmed, showing that any production of writhe is instantaneously balanced by production of twist of opposite sign so to keep helicity always zero. Moreover, as clearly shown by the plot of T29, the gradual nullification of writhe is further proof of direct topological cascade of complex structures towards the production of small-scale vortex rings. In this sense writhe measurements help to identify decaying processes.

In § 6.1 we have considered various energy contributions on isophase surfaces. By considering the surface of least geometric area (S_{min}) we have demonstrated (§ 6) that defect dynamics is actually driven by S_{min}. This is proven by considering the energy associated with S_{min}, plotting the evolution of its minimal area A_{min} against time, and showing that at each instant of time the maximal value of energy due to kinetic and quantum contributions computed on S ($\text{Max}[D(\psi)]$) corresponds to the energy computed on S_{min} ($D(\psi)|_{S_{min}}$). Plots of $A_{min} = A_{min}(t)$ (shown in figure 11) demonstrate that indeed, for all cases tested, direct topological cascade is detected by a monotonic decrease of A_{min}. The gradual decay towards the production of small, planar rings is proven by the reduction of $\chi = L^2/A$ (case T29) and it is consistent with the observed energy relaxation shown in plots of figure 12.

All this shows that non-trivial topology can indeed occur and increase during evolution; the occurrence of several reconnections at once can produce dramatic structural changes with instantaneous production of small-scale vortex rings; irreversible aspects associated with quantum hydrodynamics are well detected by time asymmetry during reconnection through picks of total curvature, and the privileged role of minimal isophase surfaces is demonstrated by detecting surface energy relaxation of natural decaying processes. As recent numerical evidence seems to suggest (Iyer, Bharadwaj & Sreenivasan 2021), our findings hint at possible interesting connections with the so-called area rule and role of minimal surfaces in classical turbulence. The energy relaxation associated with the evolution of minimal isophase surfaces provides clear evidence that also quantum defects follow the classical route to turbulence (Ruelle & Takens 1971) as shown by the cascade of complex structures towards small-scale vortex rings.

Declaration of interests. The authors report no conflict of interest.

Author ORCIDs.
 Simone Zuccher https://orcid.org/0000-0002-9057-6892;
 Renzo L. Ricca https://orcid.org/0000-0002-7304-4042.

Author contributions. R.L.R. proposed and designed the project and wrote the paper; S.Z. implemented the code and performed the simulations. All authors contributed equally to analysing data and discussing the conclusions.

References

ALLEN, A.J., ZUCCHER, S., CALIARI, M., PROUKAKIS, N.P., PARKER, N.G. & BARENGHI, C.F. 2014 Vortex reconnections in atomic condensates at finite temperature. *Phys. Rev.* A **90**, 013601.

ANDREWS, M.R., TOWNSEND, C.G., MIESNER, H.-J., DURFEE, D.S., KURN, D.M. & KETTERLE, W. 1997 Observation of interference between two Bose condensates. *Science* **275**, 637–641.

BAI, W.-K., YANG, T. & LIU, W.-M. 2020 Topological transition from superfluid vortex rings to isolated knots and links. *Phys. Rev.* A **102**, 063318.

BARENGHI, C.F. & PARKER, N.G. 2016 *A Primer on Quantum Fluids*. Springer.

BERLOFF, N.G. 2004 Padé approximations of solitary wave solutions of the Gross–Pitaevskii equation. *J. Phys. A: Math. Gen.* **37**, 11729.

BUSTAMANTE, M.D. & NAZARENKO, S. 2015 Derivation of the Biot–Savart equation from the nonlinear Schrödinger equation. *Phys. Rev. E* **92**, 053019.

CALIARI, M. & ZUCCHER, S. 2018 Reliability of the time splitting Fourier method for singular solutions in quantum fluids. *Comput. Phys. Commun.* **222**, 46–58.

CALIARI, M. & ZUCCHER, S. 2021 A fast time splitting finite difference approach to Gross–Pitaevskii equations. *Commun. Comput. Phys.* **29**, 1336–1364.

CHENG, M., LOU, J. & LIM, T.T. 2018 Numerical simulation of head-on collision of two coaxial vortex rings. *Fluid Dyn. Res.* **50**, 065513.

CLARK DI LEONI, P., MININNI, P.D. & BRACHET, M.E. 2016 Helicity, topology, and Kelvin waves in reconnecting quantum knots. *Phys. Rev. A* **94**, 043605.

COOPER, R.G., MESGARNEZHAD, M., BAGGALEY, A.W. & BARENGHI, C.F. 2019 Knot spectrum of turbulence. *Sci. Rep.* **9**, 10545.

CORNELL, E.A. & WIEMAN, C.E. 1998 The Bose–Einstein condensate. *Sci. Am.* **278**, 40–45.

COULAIS, C., FLEURY, R. & VAN WEZEL, J. 2021 Topology and broken hermiticity. *Nat. Phys.* **17**, 9–13.

COURANT, R. 1950 *Dirichlet's Principle, Conformal Mapping, and Minimal Surfaces*. Interscience Pubs.

DOS SANTOS, F.E.A. 2016 Hydrodynamics of vortices in Bose–Einstein condensates: a defect-gauge field approach. *Phys. Rev. A* **94**, 063633.

FORESTI, M. & RICCA, R.L. 2019 Defect production by pure twist induction as Aharonov–Bohm effect. *Phys. Rev. E* **100**, 023107.

FORESTI, M. & RICCA, R.L. 2020 Hydrodynamics of a quantum vortex in the presence of twist. *J. Fluid Mech.* **904**, A25.

GROSS, E.P. 1961 Structure of a quantized vortex in boson systems. *Il Nuovo Cimento* **20**, 454–457.

HALL, D.S., RAY, M.W., TIUREV, K., RUOKOKOSKI, E., GHEORGHE, A.H. & MÖTTÖNEN, M. 2016 Tying quantum knots. *Nat. Phys.* **12**, 478–483.

IYER, K.P., BHARADWAJ, S.S. & SREENIVASAN, K.R. 2021 The area rule for circulation in three-dimensional turbulence. *Proc. Natl Acad. Sci. USA* **118**, 2114679118.

KAUFFMAN, L.H. 2001 *Knots and Physics*. World Scientific.

KEDIA, H., KLECKNER, D., SCHEELER, M.W. & IRVINE, W.T.M. 2018 Helicity in superfluids: existence and the classical limit. *Phys. Rev. Fluids* **3**, 104702.

KERR, R.M. 2011 Vortex stretching as a mechanism for quantum kinetic energy decay. *Phys. Rev. Lett.* **106**, 224501.

KLECKNER, D. & IRVINE, W.T.M. 2013 Creation and dynamics of knotted vortices. *Nat. Phys.* **9**, 253–258.

KLECKNER, D., KAUFFMAN, L.H. & IRVINE, W.T.M. 2016 How superfluid vortex knots untie. *Nat. Phys.* **12**, 650–655.

LEADBEATER, M., WINIECKI, T., SAMUELS, D.C. & BARENGHI, C.F. 2001 Sound emission due to superfluid vortex reconnections. *Phys. Rev. Lett.* **86**, 1410–1413.

LEANHARDT, A.E., GÖRLITZ, A., CHIKKATUR, A.P., KIELPINSKI, D., SHIN, Y., PRITCHARD, D.E. & KETTERLE, W. 2002 Imprinting vortices in a Bose–Einstein condensate using topological phases. *Phys. Rev. Lett.* **89**, 190403.

LIM, T.T. & NICKELS, T.B. 1992 Instability and reconnection in the head-on collision of two vortex rings. *Nature* **357**, 225–227.

LIU, X. & RICCA, R.L. 2012 The Jones polynomial for fluid knots from helicity. *J. Phys. A: Math. Theor.* **45**, 205501.

LIU, X. & RICCA, R.L. 2015 On the derivation of HOMFLYPT polynomial invariant for fluid knots. *J. Fluid Mech.* **773**, 34–48.

LIU, X. & RICCA, R.L. 2016 Knots cascade detected by a monotonically decreasing sequence of values. *Sci. Rep.* **6**, 24118.

MATTHEWS, M.R., ANDERSON, B.P., HALJAN, P.C., HALL, D.S., WIEMAN, C.E. & CORNELL, E.A. 1999 Vortices in a Bose–Einstein condensate. *Phys. Rev. Lett.* **83**, 2498–2501.

MESGARNEZHAD, M., COOPER, R.G., BAGGALEY, A.W. & BARENGHI, C.F. 2018 Helicity and topology of a small region of quantum vorticity. *Fluid Dyn. Res.* **50**, 011403.

MOFFATT, H.K. 1969 The degree of knottedness of tangled vortex lines. *J. Fluid Mech.* **35**, 117–129.

MOFFATT, H.K. & RICCA, R.L. 1992 Helicity and the Călugăreanu invariant. *Proc. R. Soc. Lond.* A **439**, 411–429.

NORE, C., ABID, M. & BRACHET, M.E. 1997 Decaying Kolmogorov turbulence in a model of superflow. *Phys. Fluids* **9**, 2644–2669.

OBERTI, C. & RICCA, R.L. 2016 On torus knots and unknots. *J. Knot Theory Ramifications* **25**, 1650036.

OBERTI, C. & RICCA, R.L. 2019 Influence of winding number on vortex knots dynamics. *Sci. Rep.* **9**, 17284.

PITAEVSKII, L.P. 1961 Vortex lines in an imperfect Bose gas. *Sov. Phys. JETP* **13**, 451–54.

PITAEVSKII, L.P. & STRINGARI, S. 2016 *Bose–Einstein Condensation and Superfluidity*. Oxford University Press.

PROMENT, D., ONORATO, M. & BARENGHI, C.F. 2012 Vortex knots in a Bose–Einstein condensate. *Phys. Rev.* E **85**, 036306.

RICCA, R.L. 1998 Applications of knot theory in fluid mechanics. In *Knot Theory* (ed. V.F.R. Jones *et al.*), vol. 42, pp. 321–346. Banach Center Publs., Polish Academy of Sciences.

RICCA, R.L. 2009 New developments in topological fluid mechanics. *Nuovo Cimento* C **32**, 185–192.

RICCA, R.L. & NIPOTI, B. 2011 Gauss' linking number revisited. *J. Knot Theory Ramifications* **20**, 1325–1343.

ROLFSEN, D. 1990 *Knots and Links*. AMS Chelsea Publications.

RUELLE, D. & TAKENS, F. 1971 On the nature of turbulence. *Commun. Math. Phys.* **20**, 167–192 (see also: Note concerning our paper "On the nature of turbulence". *Commun. Math. Phys.* **23**, 343–344).

SALMAN, H. 2017 Helicity conservation and twisted Seifert surfaces for superfluid vortices. *Proc. R. Soc.* A **473**, 20160853.

SCHEELER, M.W., KLECKNER, D., PROMENT, D., KINDLMANN, G.L. & IRVINE, W.T.M. 2014 Helicity conservation by flow across scales in reconnecting vortex links and knots. *Proc. Natl Acad. Sci. USA* **111**, 15350–15355.

SHIMOKAWA, K., ISHIHARA, K., GRAINGE, I., SHERRATT, D.J. & VAZQUEZ, M. 2013 FtsK-dependent XerCD-dif recombination unlinks replication catenanes in a stepwise manner. *Proc. Natl Acad. Sci. USA* **110**, 20906.

SIGGIA, E. 1985 Collapse and amplification of a vortex filament. *Phys. Fluids* **28**, 794–805.

STOLZ, R., YOSHIDA, M., BRASHER, R., FLANNER, M., ISHIHARA, K., SHERRATT, D.J., SHIMOKAWA, K. & VAZQUEZ, M. 2017 Pathways of DNA unlinking: a story of stepwise simplification. *Sci. Rep.* **7**, 12420.

SUMNERS, D.W.L., CRUZ-WHITE, I.I. & RICCA, R.L. 2021 Zero helicity of Seifert framed defects. *J. Phys.* A*: Math. Theor.* **54**, 295203.

VILLOIS, A., PROMENT, D. & KRSTULOVIC, G. 2016 Evolution of a superfluid vortex filament tangle driven by the Gross–Pitaevskii equation. *Phys. Rev.* E **93**, 061103(R).

VILLOIS, A., PROMENT, D. & KRSTULOVICH, G. 2020 Irreversible dynamics of vortex reconnections in quantum fluids. *Phys. Rev. Lett.* **125**, 164501.

WANG, K., DUTT, A., WOJCIK, C.C. & FAN, S. 2021 Topological complex-energy braiding of non-Hermitian bands. *Nature* **598**, 59–64.

WYATT, R.E. 2005 *Quantum Dynamics with Trajectories*. Springer.

YAO, J., YANG, Y. & HUSSAIN, F. 2021 Dynamics of a trefoil knotted vortex. *J. Fluid Mech.* **923**, A19.

ZUCCHER, S. & CALIARI, M. 2021 Accurate numerical determination of a self-preserving quantum vortex ring. *J. Phys.* A*: Math. Theor.* **54**, 015301.

ZUCCHER, S., CALIARI, M., BAGGALEY, A.W. & BARENGHI, C.F. 2012 Quantum vortex reconnections. *Phys. Fluids* **24**, 125108.

ZUCCHER, S. & RICCA, R.L. 2015 Helicity conservation under quantum reconnection of vortex rings. *Phys. Rev.* E **92**, 061001.

ZUCCHER, S. & RICCA, R.L. 2017 Relaxation of twist helicity in the cascade process of linked quantum vortices. *Phys. Rev.* E **95**, 053109.

ZUCCHER, S. & RICCA, R.L. 2018 Twist effects in quantum vortices and phase defects. *Fluid Dyn. Res.* **50**, 011414.